Delft University of Technology

Permeability and Turbulence Over Perforated Plates

Shahzad, Haris; Hickel, Stefan; Modesti, Davide

Citation (APA)
Shahzad, H., Hickel, S., & Modesti, D. (2022). Permeability and Turbulence Over Perforated Plates. *Flow, Turbulence and Combustion*, *109*(4), 1241-1254. https://doi.org/10.1007/s10494-022-00337-7

Important note
To cite this publication, please use the final published version (if applicable).
Please check the document version above.

Check for
updates

Permeability and Turbulence Over Perforated Plates

Haris Shahzad[1] · Stefan Hickel[1] · Davide Modesti[1]

Abstract

We perform direct numerical simulations of turbulent flow at friction Reynolds number $Re_\tau \approx 500-2000$ grazing over perforates plates with moderate viscous-scaled orifice diameter $d^+ \approx 40 - 160$ and analyse the relation between permeability and added drag. Unlike previous studies of turbulent flows over permeable surfaces, we find that the flow inside the orifices is dominated by inertial effects, and that the relevant permeability is the Forchheimer and not the Darcy one. We find evidence of a fully rough regime where the relevant length scale is the inverse of the Forchheimer coefficient, which can be regarded as the resistance experienced by the wall-normal flow. Moreover, we show that, for low porosities, the Forchheimer coefficient can be estimated with good accuracy using a simple analytical relation.

Keywords Wall turbulence · Direct numerical simulation · Perforated plates · Permeable walls · Forchheimer permeability

1 Introduction

Turbulent flows grazing over permeable surfaces are common in engineering. Perforated plates, in particular, are used for flow conditioning (Laws and Ouazzane 1995), enhancing heat transfer in heat exchangers (Kutscher 1994), flame control in combustion chambers (Wei et al. 2017), aircraft trailing edge noise abatement (Carpio et al. 2019) and acoustic liners in aircraft engines (Casalino et al. 2018; Shur et al. 2021). Many of these applications feature turbulent grazing boundary layers over perforated plates, which result in higher drag than the baseline smooth wall. However, the drag increase is often accepted as a mandatory compromise to effectively control some other flow property, such as sound or heat transfer.

✉ Haris Shahzad
h.shahzad@tudelft.nl

Stefan Hickel
s.hickel@tudelft.nl

Davide Modesti
d.modesti@tudelft.nl

1   Aerodynamics Group, Faculty of Aerospace Engineering, Delft University of Technology, Kluyverweg 2, 2629 HS Delft, South Holland, The Netherlands

🌀 Springer

Perforated plates are substantially different from other porous surfaces, such as metal foams, ceramic filters and gravel, for example, because they are characterized by relatively larger pores with respect to the boundary layer thickness of the grazing flow, $d/\delta \approx \mathcal{O}(0.1)$ (Avallone et al. 2019). Pores with large diameter have the potential to substantially alter the flow physics compared to canonical porous surfaces which are characterized by large porosity (i.e. open-area ratio), $\sigma > 0.8$, but very small pore diameters, $d/\delta < 0.01$ and $d^+ = d/\delta_v < 20$ (Efstathiou and Luhar 2018; Manes et al. 2011), where $\delta_v = \nu/u_\tau$ is the viscous length scale, $u_\tau = \sqrt{\tau_w/\rho}$ is the friction velocity. As customary for flows over complex surface textures, τ_w is the drag per plane area, which includes both the viscous and pressure drag and ρ and ν are the fluid density and kinematic viscosity, respectively. These small pore sizes allow us to accurately model this type of surfaces using Darcy models,

$$U_{ci} = -\frac{K_{ij}}{\mu}\frac{\partial P}{\partial x_j}, \tag{1}$$

where $\partial P/\partial x_j$ is the pressure gradient across the permeable layer, K_{ij} is the permeability tensor, U_{c_i} is the characteristic velocity component in i direction, and μ is the dynamic viscosity of the fluid. Darcy permeability has the physical dimensions of an area, and it represents the ease with which flow passes through a porous surface. The Darcy law (1) stems from the momentum balance of the Navier–Stokes equations, and it is usually considered an accurate model of canonical porous surfaces, at least when the Reynolds number based on the pore diameter is small enough that the underlying Stokes approximation remains valid.

Several authors have used Darcy's boundary conditions to model the turbulent flow over porous substrates (Rosti et al. 2018; Li et al. 2020) and reported accurate results as compared to pore-resolved simulations (Kuwata and Suga 2017). With the exception of some particular configurations (Gómez-de-Segura and García-Mayoral 2019), porous surfaces tend to increase drag, similar to surface topography. (Manes et al. 2009; Manes et al. 2011) discussed the similarities and differences between canonical porous surfaces and roughness and concluded that porous surfaces interact differently with the grazing flow as compared to rough surfaces. Breugem et al. (2006), for instance, report that porous surfaces do not exhibit a fully rough regime in which the skin-friction coefficient approached a constant value with increasing Reynolds number.

The added drag provided by rough surfaces is characterized by the roughness Reynolds number $k^+ = k/\delta_v$, where k is the roughness height. Hence, k is usually regarded as the surface length scale to be compared with the viscous length scale, δ_v, to determine whether the flow is strongly affected by the surface roughness. For porous surfaces, two types of length scales have generally been considered, namely the pore size d and the square root of the permeabilities $\sqrt{K_{ij}}$, but several authors have shown that drag depends on the dominant viscous-scaled permeability component, or a combination of $\sqrt{K_{ij}}^+ = \sqrt{K_{ij}}/\delta_v$ (Gómez-de-Segura and García-Mayoral 2019; Rosti et al. 2018; Breugem et al. 2006).

Equation (1) has been proven to be accurate for many canonical porous surfaces, and it is applicable within the limit of Stokes flow, namely for small values of the pore Reynolds number $Re_p = \rho d U_p/\mu$, where U_p is the velocity inside the pore. However, deviations from Darcy's law for increasing Re_p are well documented in the literature (Tanner et al. 2019; Bae and Kim 2016; Lee and Ih 2003), and have been associated with nonlinear effects that arise at high pore Reynolds numbers. Re_p is higher for perforated plates than for other porous surfaces and therefore Eq. (1) is replaced by,

$$\frac{\Delta P}{t}\frac{d^2}{\mu U_t} = \frac{d^2}{K_y} + \sigma\alpha_y dRe_p, \tag{2}$$

where U_t is the superficial velocity (Fig. 1a), t is the thickness of the plate and K_y and α_y are the permeability and the Forchheimer coefficient in the direction normal to the plate, respectively (Lee and Ih 2003; Bae and Kim 2016). The superficial velocity is the hypothetical uniform incoming velocity perceived by the orifice (Tanner et al. 2019). This is related to the orifice velocity by mass conservation,

$$U_t A_p = U_p A_o \quad \Rightarrow \quad U_t = \sigma U_p, \quad \sigma = \frac{A_o}{A_p}, \tag{3}$$

where A_p and A_o are the plate and the orifice area, respectively. Hence, the superficial velocity can be interpreted as measure of the total mass flow rate through the permeable surface.

Figure 1b shows the contribution of the Darcy and Forchheimer terms to the normalized pressure drop as a function of the pore Reynolds number. It is evident that nonlinear effects start already at low values of $Re_p \approx 5$ and become dominant at $Re_p \approx 50$.

At sufficiently high pore Reynolds number, Darcy drag can be assumed negligible and the entirety of the pressure drag is due to the nonlinear term. The pressure drop characteristics of perforated plates at high Reynolds numbers $Re_p \geq \mathcal{O}(10^2)$ have been studied extensively both numerically (Tanner et al. 2019) and experimentally (Idelchik 1994; Kast et al. 2010; Malavasi et al. 2012; Miller 1990; Holt et al. 2011); however Eq. (2) for the normal flow has never been associated to the case of grazing boundary layer over porous surfaces, for which Darcy's law has always been used, to our knowledge.

In this study, we aim at clarifying the errors that potentially result from using Eq. (1) for grazing turbulent boundary layers over perforated plates, and, in particular, from using the square root of the Darcy permeability as a relevant length scale. First, we perform simulations of laminar flow through perforated plates to compute the Darcy and the Forchheimer permeability coefficients and compare the results with experimental and numerical data, and with popular engineering approximations. Second, we carry out direct numerical simulation (DNS) of turbulent channel flow grazing over perforated walls and discuss the relevance of the Forchheimer coefficient for the drag of this flow.

Fig. 1 **a** Sketch of the flow normal to a perforated plate with diameter d and thickness t. U_t is the superficial velocity and $\Delta P = P_1 - P_2$ the pressure drop through the plate. **b** Darcy (blue) and Forchheimer (red) contributions to the pressure drop from Eq. (2) as a function of the pore Reynolds number Re_p for $\sigma = 0.322$ and $t/d = 1$
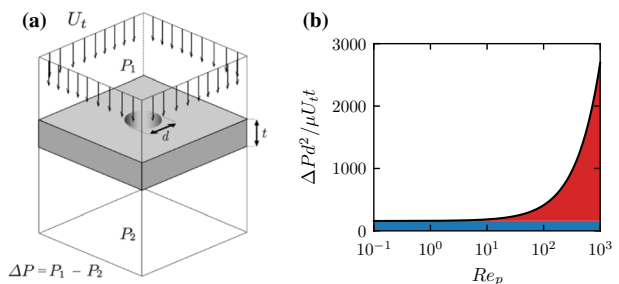
2 Flow through a Perforated Plate

In order to calculate the Darcy and Forchheimer coefficients, we perform simulations of laminar flow through a perforated plate using the setup sketched in Fig. 1. We solve the incompressible Navier–Stokes equations, and fix the superficial velocity at the inflow and the pressure at the outflow. Neumann boundary conditions are used for the outflow velocity and inflow pressure. No-slip boundary condition is used at the surface of the perforated plate, and symmetry boundary conditions are used at the lateral boundaries.

Simulations discussed in this section are performed with the pimpleFoam solver, which is part of the open-source library OpenFOAM® (Weller et al. 1998). A forward Euler time step scheme with a maximum CFL number of 0.7 is used and simulations are run until a steady-state solution is reached (residual $< 10^{-9}$). The inflow and outflow boundaries are at least 40 orifice diameters away from the perforated plate. We have verified that the final solution is independent of the domain size. Approximately 10 M cells are used with a minimum mesh size of $\approx 0.001d$ in the proximity of the plate orifice. We have performed a grid resolution study to ensure that the presented results are fully converged.

We consider 9 plate geometries with different porosity and thickness-to-diameter ratio t/d, which are summarised in Table 1. Six geometries are designed to match the parameters of Bae and Kim (2016) ($B_{r1} - B_{r3}$), and Tanner et al. (2019) ($T_{r1} - T_{r3}$), whereas ($L_{g1} - L_{g3}$) are novel geometries. Permeability is considered independent of the spacing of the holes (Bae and Kim 2016; Malavasi et al. 2012; Tanner et al. 2019), therefore we simulate plates with a single orifice, and change the porosity by changing the orifice diameter. The pressure drop ΔP is evaluated as the difference between the inlet and outlet pressure, see the sketch in Fig. 1a. For each of the 9 plate geometries, we perform simulations at different Re_p and use Eq. (2) to compute the Darcy permeability and the Forchheimer coefficient.

Figure 2 shows the pressure drop of flow cases $B_{r1} - B_{r3}$(**a**) and $T_{r1} - T_{r3}$(**b**) for our simulations and corresponding data from Bae and Kim (2016) and Tanner et al. (2019). We note a disagreement for flow cases $B_{r1} - B_{r3}$ when compared to the data of Bae and Kim (2016), which becomes more evident for increasing pore Reynolds number, with

Table 1 Forchheimer coefficient for different porosities σ and thickness-to-diameter ratio t/d. The last column refers to the present dataset, whereas the other columns refer to the values obtained with engineering correlations reported in the Appendix 1

	σ	t/d	$\alpha_y d$						
			Kast et al. (2010)	Idelchik (1994)	Malavasi et al. (2012)	Miller (1990)	Holt et al. (2011)	Bae and Kim (2016)	Present
B_r1	0.2	2	12.3	6.59	12.5	6.55	4.82	7.5	7.68
B_r2	0.3	2	4.69	2.36	4.62	2.35	1.75	2.91	4.67
B_r3	0.4	2	2.25	1.05	2.07	1.02	0.791	1.41	2.61
T_r1	0.2	0.25	98.0	94.9	100	247	89.9	60.0	70.2
T_r2	0.4	0.25	18.0	15.2	16.6	38.5	13.4	11.2	13.17
T_r3	0.6	0.25	5.55	3.69	3.91	8.28	3.69	3.33	4.43
L_g1	0.0357	1	960	643	1005	644	604	567	763
L_g2	0.143	1	51.9	33.1	53.8	33.6	25.0	31.4	46.2
L_g3	0.322	1	7.89	4.51	7.59	3.95	3.00	4.91	7.87
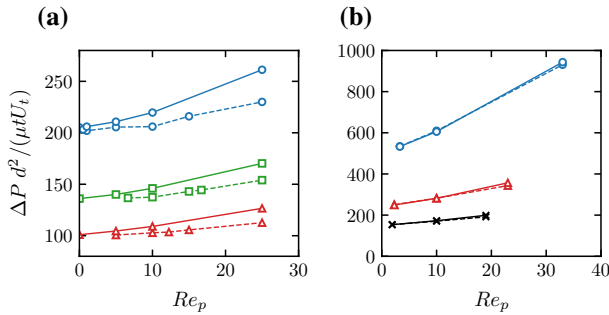
Fig. 2 Normalised pressure drop as a function of the pore Reynolds number for cases B_{r1}-B_{r3} (**a**) and cases T_{r1}-T_{r3} (**b**). Solid lines represent pressure drop for the current simulations. Dashed lines represent the pressure drops by Bae and Kim (2016) and Tanner et al. (2019) in (**a**) and (**b**), respectively. Symbols refer to different porosities: $\sigma = 0.2$ (circles), $\sigma = 0.3$ (squares), $\sigma = 0.4$ (triangles) and $\sigma = 0.5$ (crosses)

differences up to 20% at the highest Re_p. On the contrary, we observe a very good match for flow cases $T_{r1} - T_{r3}$ with the data of Tanner et al. (2019). The reasons for the mismatch between the two datasets can be numerous, but are most likely down to the different flow solver and numerical set up. For example, an upwind scheme was used by Bae and Kim (2016), whereas a second-order central discretization scheme is used for the present simulations. Discrepancies of this order of magnitude are possible at high Re_p (Malavasi et al. 2012), and therefore we consider the differences acceptable.

As additional validation, we compare the Forchheimer coefficients from the current simulations to several engineering correlations based on experimental data, which are summarized in Appendix 1. The values of α_y returned by these correlations are reported in Table 1. There is a large spread in the Forchheimer coefficient proposed by the different correlations, and differences up to $50 - 60\%$ seem common in the literature.

This large uncertainty of the Forchheimer coefficient can be traced back to the weak dependence of α_y on Re_p, which has been reported by several studies (Tanner et al. 2019). Most of these empirical correlations are based on data at high pore Reynolds numbers in the attempt to minimize the dependence on Re_p. However, this is often not enough because the dependence of α_y on Re_p can be more or less significant depending on the thickness-to-diameter ratio t/d (Tanner et al. 2019), thus complicating the evaluation of the Forchheimer coefficient. Perfect agreement with the empirical correlations is therefore not expected. The Forchheimer coefficients we calculate are within the range of the engineering correlations (50%-60% spread, Table 1), that are based on experimental data at high Reynolds number. Comparison with previous numerical simulations in Fig. 2, show a much better agreement with our data.

Even though these correlations differ from each other, they all suggest the same trend of the Forchheimer coefficient for low values of σ, namely $\alpha_y \sim 1/(\sigma^2 t)$. For this reason, we report $\alpha_y d$ as a function of $\sigma^2 t/d$ in Fig. 3. The figure shows a visual representation of the Forchheimer coefficient which highlights that the dependence of α_y on the geometry is approximately captured with a single geometrical parameter. The approximation $\alpha_y \sim 1/(\sigma^2 t)$ is accurate for lower values of the porosity, whereas we observe larger errors for large σ. For low values of the porosity $\sigma < 0.2$ this simple analytical formula has comparable accuracy as experimental data.

Fig. 3 Forchheimer coefficient $\alpha_y d$ as a function of $\sigma^2 t/d$ for L_{g1} -L_{g3} (circles), B_{r1}-B_{r3} (squares) and T_{r1}-T_{r3} (triangles)
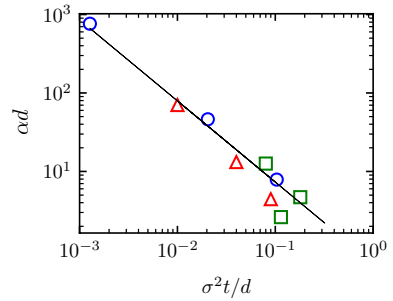
3 Turbulent flow over perforated plates

In this section, we present DNS results of turbulent grazing flow over perforated plates for different porosities and Reynolds numbers. Even though perforated plates are an elementary porous surface in terms of geometry, several configurations are in principle possible. Here, we consider geometries that resemble the acoustic liners used within aircraft engines, which consist of a perforated facesheet and a solid backplate with a honeycomb in between. Acoustic liners have an orifice diameter of about $d/\delta \approx 0.1$ and a honeycomb depth $h/\delta = 2$, a porosity in the range $\sigma = 0.05 - 0.3$, and a plate thickness of $t/d \approx 1$.

3.1 Methodology

For the DNS, we solve the compressible Navier–Stokes equations for a perfect gas using the flow solver STREAmS (Bernardini et al. 2021). The simulations are carried out in a rectangular box of size $L_x \times L_y \times L_z = 3\delta \times 3\delta \times 1.5\delta$, where δ is the channel half-width and x, y and z are the streamwise, wall-normal and spanwise directions, respectively. This box size is smaller than the one typically recommended for achieving domain independence on smooth walls (Lozano-Durán and Jiménez 2014), however, even smaller box sizes have been used successfully for studying flows over rough walls (Chung et al. 2015; MacDonald et al. 2017; Di Giorgio et al. 2020; Yang et al. 2022). The main idea is that when studying the flow over roughness or porous surfaces, one is interested in comparing results with a baseline smooth configuration, therefore the effect of the box size is minimized if results are compared to smooth-wall simulations with the same computational domain. The simulations are performed at bulk Mach number, $M_b = u_b/c_w = 0.3$, where u_b is the bulk flow velocity and c_w is the speed of sound at the wall. At this Mach number, compressibility effects are very small, and the flow can be regarded as representative of incompressible turbulence. The flow is driven in the streamwise direction by a spatially uniform body force, adjusted every time step to keep a constant bulk velocity u_b.

Periodic boundary conditions are applied in the streamwise and spanwise directions and no-slip isothermal boundary conditions are applied at the wall using a ghost-point immersed boundary method (Vanna et al. 2020). The orifice diameter is resolved with approximately 40 grid points in the streamwise and spanwise direction.

We choose the liner geometry to match the orifice size of acoustic liners in operating conditions as close as possible. The acoustic liner comprises of 64 cavities: an array of 8×4 in the streamwise and spanwise direction on the upper and lower wall. Each cavity

Table 2 DNS dataset comprising smooth, (S_n) and liner (L_n) cases. σ is the porosity (open area ratio), d^+ is the orifice diameter, K_y is the Darcy permeability, α_y is the Forchheimer coefficient and ΔU^+ is the Hama roughness function. Simulations are performed in computational a box with dimensions $L_x \times L_y \times L_z = 3\delta \times 3\delta \times 1.5\delta$

	Re_b	Re_τ	d^+	t/d	σ	$\sqrt{K_y}^+$	$1/\alpha_y^+$	ΔU^+	Δx^+	Δy_{min}^+	Δy_{max}^+	Δz^+
S_1	9268	506.1	0	0	0	0	0	–	5.1	0.80	3.83	5.1
S_2	21,180	1048	0	0	0	0	0	–	5.2	0.80	4.45	5.2
S_3	45,240	2060	0	0	0	0	0	–	5.2	0.80	6.67	5.2
L_1	9139	503.5	40.3	1	0.0357	1.04	0.0528	0.14	1.1	0.80	5.81	1.1
L_2	8794	496.4	39.7	1	0.142	2.06	0.859	0.56	1.0	0.80	5.81	1.0
L_3	8264	505.3	40.4	1	0.322	3.22	5.14	1.90	1.0	0.81	5.81	1.0
L_4	19,505	1038	83.0	1	0.142	4.30	1.718	0.96	2.1	0.83	6.30	2.1
L_{u4}	19,505	1044	83.5	1	0.142	4.32	1.727	0.98	5.9	0.84	6.10	5.9
L_5	17,810	1026	82.1	1	0.322	6.53	10.4	2.78	2.1	0.82	6.29	2.1
L_6	35,470	2044	164.0	1	0.322	13.0	20.8	4.44	4.1	0.82	6.70	4.1

Δx^+ and Δz^+ are the viscous-scaled mesh spacing in the streamwise and spanwise direction. Δy_{min}^+ and Δy_{max}^+ are the minimum and the maximum mesh spacing in the wall normal direction. Liner cases (L_1)–(L_6) have equispaced orifices in the streamwise and spanwise direction. Case L_{u4} has the same porosity, and orifice size of L_4 but the holes are not equispaced in the streamwise direction, Fig. 5

has a square cross-section with a side length $\lambda = 0.375\delta$, the orifices have a diameter of $d = 0.08\delta$, the cavity walls have a thickness of $0.5d$, and the facesheet has a thickness of d. The cavities have a depth $h = 0.5\delta$, which is smaller than the one of typical acoustic liners. However, the cavity depth only plays a role for tuning sound attenuation and not for the aerodynamic drag Howerton and Jones (2015).

We carry out simulations at three friction Reynolds numbers in the range $Re_\tau = \delta/\delta_v \approx 500 - 2000$, corresponding to a viscous-scaled diameter of $d^+ \approx 40 - 160$. Additionally, we increase the liner porosity between $\sigma = 0.0357 - 0.322$ by varying the number of orifices per cavity between 1 and 9. An instantaneous flow visualisation of flow case L_6 is shown in Fig. 4. Figure 4 shows the arrangements of the cavities on the upper and lower walls and also visualises the vortical structures with the aid of the Q-criterion.

Fig. 4 Instantaneous flow field for flow case L_6 at $Re_\tau = 2000$ and bulk Mach number $M_b = 0.3$. Vortical structures are visualised using the Q-Criterion

Flow Direction
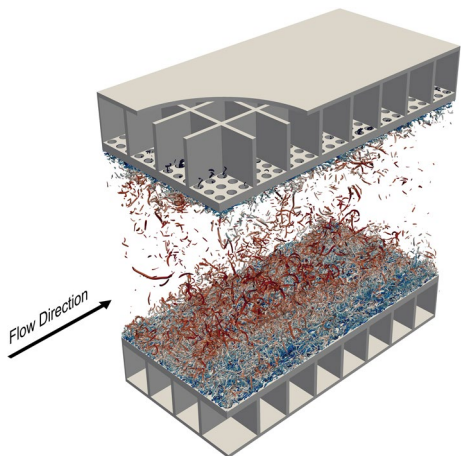
Fig. 5 Sketch the holes arrangement in the wall-parallel plane for the DNS cases. Panels (**a**), (**b**) and (**c**) correspond to cases L_{r1}, L_{r2} and L_{r3}, respectively. Geometries (**a**), (**b**) and (**c**) have equispaced holes. Geometry (**d**) has the same orifice diameter, plate thickness and porosity as (**b**), but the orifices are not evenly spaced
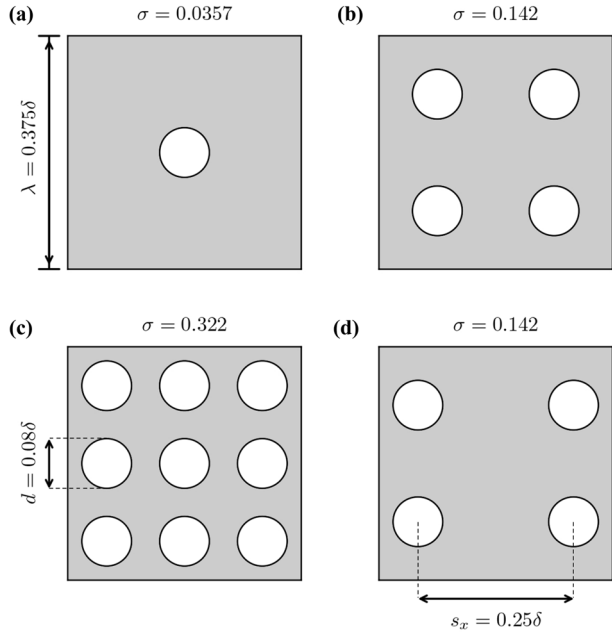

The geometries considered are visualised in Fig. 5 and the complete list of flow cases is reported in Table 2. We also change the spacing between the orifices, flow cases L_4 and L_{u4} (Figs. 5b, d). We compare the results of the liner simulations with smooth-wall simulations at approximately matching friction Reynolds numbers. Quantities normalized in viscous units are denoted with the '+' superscript, where δ_v and u_τ are based on the drag per plane area of the corresponding flow case.

3.2 Added drag and permeability

As customary for turbulent flows over rough and porous surfaces, we quantify the added drag with respect to the smooth wall using the viscous-scaled velocity deficit in the logarithmic region ΔU^+, also referred to as Hama roughness function (Chung et al. 2021). For our geometries, we consider three candidate Reynolds numbers for scaling ΔU^+, namely based on the orifice diameter d^+, based on the square root of the wall-normal permeability $\sqrt{K_y}^+$ and based on the inverse of the Forchheimer coefficient $1/\alpha_y^+$.

Figure 6a shows ΔU^+ as a function of the viscous-scaled diameter. It is clear that d^+ alone is not a suitable similarity parameter because increasing the surface porosity for a constant viscous-scaled orifice diameter leads to higher ΔU^+. For instance, cases L_2 and L_3 have approximately matching d^+, but case L_3 exhibits a larger ΔU^+ owing to the higher porosity.

Figure 6b shows ΔU^+ as a function of the viscous-scaled wall-normal Darcy permeability. The Darcy coefficient is also not suitable for predicting the drag increase as it does not show a consistent monotonic trend. Instead, we find that the inverse of the viscous-scaled Forchheimer coefficient $1/\alpha_y^+$ scales very well the effect of the liner, as shown in Fig. 7a. We clearly see that $1/\alpha_y^+$ is a promising length scale for characterising the additional drag.
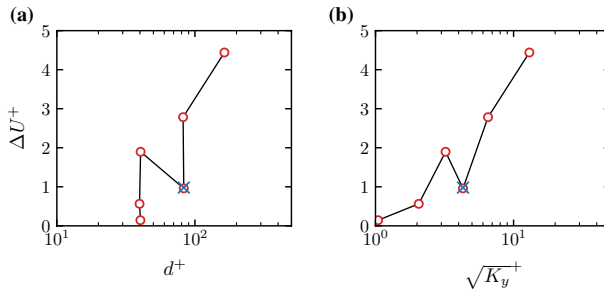
Fig. 6 ΔU^+ as a function of the viscous-scaled orifice diameter, d^+ (**a**) and the Darcy permeability (**b**). Equispaced orifice cases are represented by circles. Non-equispaced orifices case is represented by a cross
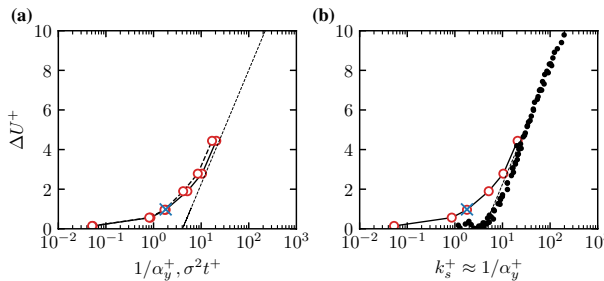

Fig. 7 ΔU^+ as a function of the inverse of the Forchheimer coefficient, $1/\alpha_y^+$ (solid line) and $\sigma^2 t$ (dashed line) (**a**) and comparison with the sandgrain roughness data of Nikuradse (Nikuradse et al. 1933, filled circles) (**b**). The dotted line indicates the fully rough asymptote $\kappa^{-1}\ln(1/\alpha_y^+) - 3.5$. Equispaced orifice cases are represented by circles. Non-equispaced orifices case is represented by a cross

We note that the Hama roughness function tends towards the fully rough regime, and flow case L_6 lies on the lower edge of the asymptote $\Delta U^+ \approx \kappa^{-1}\ln(1/\alpha_y^+) - 3.5$, where κ is the von Kármán constant. Furthermore, Table 2 shows that case L_{u4} has a nearly identical ΔU^+ to case L_4. The spacing of the orifices, therefore, has a no effect and the added drag is only a function of $1/\alpha_y^+$, which provides further evidence that the Forchheimer coefficient is the relevant length scale. Figure 7b shows ΔU^+ of the liner cases as a function of $1/\alpha_y^+$, compared to Nikuradse data of sandgrain roughness (Nikuradse et al. 1933), which suggest that acoustic liners behave like sandpaper, as $1/\alpha_y^+ \approx k_s$.

Additionally, we test the accuracy of the semi-empirical scaling introduced in Sect. 2, $\alpha_y \approx 1/(\sigma^2 t)$, and we plot ΔU^+ as a function of $\sigma^2 t^+$ in Fig. 7a. The empirical correlation is very accurate for low values of $\sigma^2 t^+$, whereas minor discrepancies appear as ΔU^+ approaches the fully rough regime. This is due to the approximate correlation of the Forchheimer coefficient with $1/(\sigma^2 t)$, as can also be observed from the formulas in Appendix 1.

Both the Darcy permeability and the Forchheimer coefficient are suitable candidates to be considered as relevant length scales because they incorporate the effect of changes in the geometry. However, the Forchheimer coefficient clearly shows superior accuracy for the flow cases under scrutiny. This can be associated with the relevance of inertial effects inside the orifices, as we qualitatively show in Fig. 8 where we report the

Fig. 8 Wall-normal velocity fluctuations in a $x-y$ plane at for flow case L_5 (**a**) at $Re_\tau \approx 1000$ and flow case L_6 (**b**) at $Re_\tau \approx 2000$. Panel (**c**) shows a zoomed in version of (**b**) near the first two cavities of the lower wall to highlight the jet-like flow inside the orifices. Grey patches represent solid wall regions
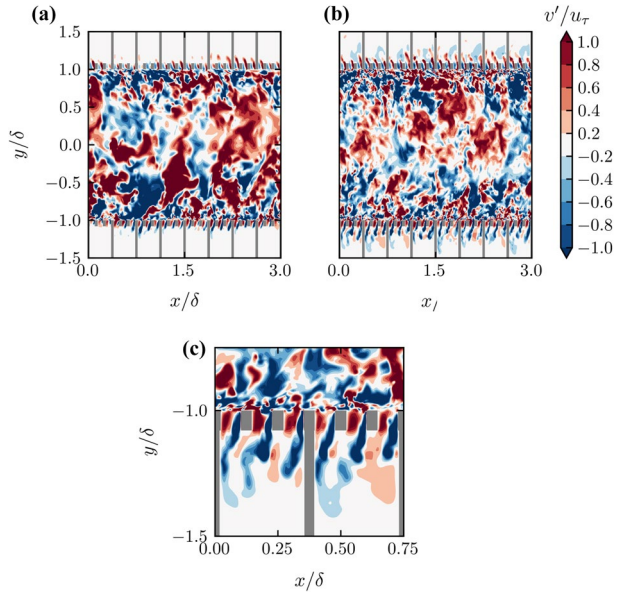
instantaneous wall-normal velocity for cases L_5 and L_6 in a x-y plane. We observe very high wall-normal velocities inside the orifices forming a jet-like flow from the downstream edge of the orifice into the cavity, which is particularly evident for flow case L_6 as fluid is pushed further inside the cavity. Inertial flow penetrating the cavities is evident in Fig. 8c, which suggests that high-wall normal velocity fluctuations below the facesheet are a strong feature characterizing this flow.

Using the maximum wall normal velocity fluctuation v_{rms} inside the orifice, we estimate a pore Reynolds number $Re_p \approx 50 - 500$, depending upon the flow case considered. The Forchheimer drag constitutes about 50% of the total drag at $Re_p \approx 50$ and almost the entirety of the drag at $Re_p \approx 500$, see Fig. 1b. This is further confirmation for the use of the Forchheimer coefficient rather than the Darcy permeability as the relevant length scale for the present flow cases.

To further clarify on the relevance of the nonzero wall-normal velocity on ΔU^+ we recall that the pressure drop through the plate can be expressed in the form of friction factor in the wall-normal direction,

$$f_y = \frac{\Delta P}{0.5\rho U_t^2}. \tag{4}$$

In the limit of high Reynolds number, the entirety of the pressure drop can be attributed to the Forchheimer pressure drop. In such a case, Eq. (2) simplifies to

$$\frac{\Delta P}{t} \frac{d^2}{\mu U_t} = \sigma \alpha_y d Re_p, \tag{5}$$

Substitution of ΔP from Eq. (5) into Eq. (2) leads to an expression for the Forchheimer coefficient as a function of the friction factor,

$$\alpha_y = \frac{f_y}{2t}. \tag{6}$$

Hence, $1/\alpha_y$ represents the drag experienced by the flow normal to the plate, suggesting that ΔU^+ is intrinsically related to the wall-normal velocity fluctuations. This result is consistent with previous studies on rough surfaces that discuss the correlation between drag and wall-normal velocity fluctuations (Orlandi et al. 2006), and it reveals several similarities between roughness and porous surfaces, which have not been reported in the literature so far.

4 Concluding remarks

We have analysed the correlation between wall-normal permeability and wall-parallel drag in turbulent flows over perforated plates. Perforated plates are different from other types of porous surfaces because their porosity does not exceed $\sigma \approx 0.3$ in most engineering applications, as higher values would substantially affect the structural integrity of the plate. Another main difference with respect to other porous surfaces is that the pore Reynolds number can be large, and in many applications, $Re_p \sim \mathcal{O}(10^2)$ or higher. The result is that the Darcy equation does not hold because inertial effects inside the orifice are dominant, and the ease with which the fluid passes through the plate is better represented by the Forchheimer coefficient than by the Darcy permeability.

Accurate calculation of the Forchheimer coefficient for perforated plates is challenging, and discrepancies up to 50% are common in the literature, both from numerical and experimental sources. We calculate the Forchheimer coefficient using numerical simulations, and our results are in good agreement with a subset of the available data and engineering correlations. Semi-empirical relations for estimating the Forchheimer coefficient often show a complex dependence on the plate geometry. However, we note that in the limit of small porosity all correlations return the same functional dependence $\alpha_y \sim 1/\sigma^2 t$, which can be used as a first-order approximation.

In order to show the practical relevance of the Forchheimer coefficient in a realistic engineering application, we carry out direct numerical simulation of turbulent grazing flow over perforated plates, which resemble the acoustic liners used for noise attenuation over aircraft engines. We show that the inverse of the viscous-scaled Forchheimer coefficient $1/\alpha_y^+$ is the relevant inner Reynolds number for this type of surface, and the Hama roughness function shows clear evidence of a fully rough regime. Moreover, these perforated plates provide the same drag as sandgrain roughness with $k_s^+ \approx 1/\alpha_y^+$. The ability of $1/\alpha_y^+$ to represent the drag of the plate is attributed to the high values of the pore Reynolds number based on the wall-normal velocity fluctuations $Re_p = 50 - 500$, which suggest dominant inertial effects inside the orifice. The high r.m.s wall-normal velocity is immediately noted in the instantaneous flow visualisations.

We believe that this study sheds new light on to the interactions of a turbulent boundary layer flow with porous surfaces. We have identified the inverse of Forchheimer coefficient as a highly relevant scaling parameter, and future efforts should be directed towards an accurate numerical characterization of this length scale, both experimentally and computationally. Last but not least, we note that our findings have been verified for a considerably large data set, however, this data can cover only a fraction of the vast parameter space. We considered the effect of the porosity and orifice diameter. Their combined effect is incorporated into both the linear and non-linear permeability

of which the latter is found to be relevant for acoustic liners. Despite the relatively simple geometry, there are at least three other free parameters defining acoustic liners, namely the cavity depth, the facesheet thickness, and the cavity length and width. Future studies should certainly explore the wider parameter space of possible geometries, however, we can make some considerations based on the present results. Previous studies have addressed the effect of the cavity depth and reported no measurable change in drag (Howerton and Jones 2015), however, DNS with deeper cavities would be desirable to confirm these findings. We expect that the thickness of the facesheet could influence the added drag, and affect the relation with the sand-grain roughness height. For the geometry under scrutiny, we found $k_s^+ \approx 1/\alpha_y^+$, but in general one could have a proportionality relation $k_s^+ = C/\alpha_y^+$, similarly to what happens for different roughness geometries. As for the effect of the cavity partitions, we expect them to have a negligible effect on our conclusions, unless such modifications induce relevant streamwise and spanwise permeabilities, which can then compete with the wall-normal one for the role of relevant length scale for the flow.

Appendix A Empirical Correlations for Pressure Drop through Perforated Plates

In this Appendix we report popular engineering formulas for estimating the Forchheimer coefficient or the friction factor.

Bae and Kim (2016) performed numerical simulations of flow through perforated plates and, proposed the following expression for the Forchheimer coefficient:

$$\alpha_y = \frac{3(1-\sigma)}{4\sigma^2 t}. \tag{A1}$$

Several experimental studies at high Reynolds number are available which provide semi-empirical formulas for the friction factor, which can be easily converted into Forchheimer coefficient using Eq. (6). Idelchik (1994) provides several empirical correlations for estimating the friction factor across a perforated plate. At finite thickness of the plate and high Reynolds number, Idelchik (1994) proposes a correlation of the form:

$$\alpha_y = \frac{1}{2\sigma^2 t}\Big(0.5 + 0.24\sqrt{1-\sigma}(1-\sigma) + (1-\sigma)^2\Big). \tag{A2}$$

Malavasi et al. (2012) suggest an alternative relationship of the form:

$$\alpha_y = \frac{1}{2C^2\sigma^2 t}\Big(\sqrt{1-\sigma^2 - \sigma^2 C^2} - C\sigma\Big)^2, \tag{A3}$$

where C is a discharge coefficient that depends upon the geometrical parameters of the orifice and the Reynolds number. Similarly, Kast et al. (2010) proposes the following relationship:

$$\alpha_y = \frac{1}{2\sigma^2 t}\bigg(\Big(\frac{1}{C}-1\Big)^2 + (1-\sigma)^2\bigg). \tag{A4}$$

According to Miller (1990) the Forchheimer coefficient can be expressed as:

$$\alpha_y = \frac{C_0(1 - C_c\sigma)}{C_c^2\sigma^2 t}, \tag{A5}$$

where C_0 is a coefficient that depends on t/d and C_c is the jet contraction coefficient. Holt et al. (2011) present a piecewise function for the Forchheimer coefficient,

$$\alpha_y = \begin{cases} \frac{1}{2t}\left(2.9 - 3.79\frac{t}{d}\sigma^{0.2} + 1.79\left(\frac{t}{d}\right)^2\sigma^{0.4}\right)K & \frac{t}{d}\sigma^{0.2} < 0.9 \\ \frac{1}{2t}\left(0.876 - 0.069\frac{t}{d}\sigma^{0.2}\right)K & \frac{t}{d}\sigma^{0.2} > 0.9, \end{cases}$$

where $K = 1 - 2/\sigma + 2/\sigma^2(1 - 1/C_C + 1/(2C_C^2))$.

Declarations

References

Avallone, F., Manjunath, P., Ragni, D., Casalino, D.: Lattice-Boltzmann very large eddy simulation of a multi-orifice acoustic liner with turbulent grazing flow. https://doi.org/10.2514/6.2019-2542

Bae, Y., Kim, Y.I.: Numerical modeling of anisotropic drag for a perforated plate with cylindrical holes. Chem. Eng. Sci. **149**, 78–87 (2016). https://doi.org/10.1016/j.ces.2016.04.036

Bernardini, M., Modesti, D., Salvadore, F., Pirozzoli, S.: Streams: A high-fidelity accelerated solver for direct numerical simulation of compressible turbulent flows. Comput. Phys. Commun. **263**, 107906 (2021). https://doi.org/10.1016/j.cpc.2021.107906

Breugem, W.P., Boersma, B.J., Uittenbogaard, R.E.: The influence of wall permeability on turbulent channel flow. J. Fluid Mech. **562**, 35–72 (2006). https://doi.org/10.1017/S0022112006000887

Carpio, A.R., Avallone, F., Ragni, D., Snellen, M., van der Zwaag, S.: Mechanisms of broadband noise generation on metal foam edges. Phys. Fluids **31**(10), 105110 (2019). https://doi.org/10.1063/1.5121248

Casalino, D., Hazir, A., Mann, A.: Turbofan broadband noise prediction using the lattice Boltzmann method. AIAA J. **56**(2), 609–628 (2018)

Chung, D., Chan, L., MacDonald, M., Hutchins, N., Ooi, A.: A fast direct numerical simulation method for characterising hydraulic roughness. J. Fluid Mech. **773**, 418–431 (2015)

Chung, D., Hutchins, N., Schultz, M.P., Flack, K.A.: Predicting the drag of rough surfaces. Annu. Rev. Fluid Mech. **53**(1), 439–471 (2021). https://doi.org/10.1146/annurev-fluid-062520-115127

Di Giorgio, S., Leonardi, S., Pirozzoli, S., Orlandi, P.: On the relationship between drag and vertical velocity fluctuations in flow over riblets and liquid infused surfaces. Int. J. Heat Fluid Flow **86**, 108663 (2020). https://doi.org/10.1016/j.ijheatfluidflow.2020.108663

Efstathiou, C., Luhar, M.: Mean turbulence statistics in boundary layers over high-porosity foams. J. Fluid Mech. **841**, 351–379 (2018)

Gómez-de-Segura, G., García-Mayoral, R.: Turbulent drag reduction by anisotropic permeable substrates - analysis and direct numerical simulations. J. Fluid Mech. **875**, 124–172 (2019). https://doi.org/10.1017/jfm.2019.482

Holt, G.J., Maynes, D., Blotter, J.: Cavitation at Sharp Edge Multi-Hole Baffle Plates. ASME IMECE, pp. 401–410 (2011). https://doi.org/10.1115/IMECE2011-64203

Howerton, B.M., Jones, M.G.: Acoustic Liner Drag: A Parametric Study of Conventional Configurations. In: AIAA Paper 2015-2230 (2015). https://doi.org/10.2514/6.2015-2230

Idelchik, I.E.: Handbook of Hydraulic Resistance, 2nd edn. CRC, Boca Raton, FL (1994)

Kast, W., Nirschl, H., Gaddis, E.S., Wirth, K.-E., Stichlmair, J.: L1 Pressure Drop in Single Phase Flow. Springer, Berlin, Heidelberg (2010). https://doi.org/10.1007/978-3-540-77877-6_70

Kutscher, C.F.: Heat exchange effectiveness and pressure drop for air flow through perforated plates with and without crosswind. J. Heat Transf. **116**(2), 391–399 (1994). https://doi.org/10.1115/1.2911411

Kuwata, Y., Suga, K.: Direct numerical simulation of turbulence over anisotropic porous media. J. Fluid Mech. **831**, 41–71 (2017). https://doi.org/10.1017/jfm.2017.619

Laws, E.M., Ouazzane, A.K.: A further investigation into flow conditioner design yielding compact installations for orifice plate flow metering. Flow Meas. Instrum. **6**(3), 187–199 (1995). https://doi.org/10.1016/0955-5986(95)00007-9

Lee, S.-H., Ih, J.-G.: Empirical model of the acoustic impedance of a circular orifice in grazing mean flow. J. Acoust. Soc. Am. **114**(1), 98–113 (2003). https://doi.org/10.1121/1.1581280

Li, Q., Pan, M., Zhou, Q., Dong, Y.: Turbulent drag modification in open channel flow over an anisotropic porous wall. Phys. Fluids **32**(1), 015117 (2020). https://doi.org/10.1063/1.5130647

Lozano-Durán, A., Jiménez, J.: Effect of the computational domain on direct simulations of turbulent channels up to re $\tau = 4200$. Phys. Fluids **26**(1), 011702 (2014)

MacDonald, M., Chung, D., Hutchins, N., Chan, L., Ooi, A., García-Mayoral, R.: The minimal-span channel for rough-wall turbulent flows. J. Fluid Mech. **816**, 5–42 (2017)

Malavasi, S., Messa, G., Fratino, U., Pagano, A.: On the pressure losses through perforated plates. Flow Meas. Instrum. **28**, 57–66 (2012). https://doi.org/10.1016/j.flowmeasinst.2012.07.006

Manes, C., Pokrajac, D., McEwan, I., Nikora, V.: Turbulence structure of open channel flows over permeable and impermeable beds: A comparative study. Phys. Fluids **21**(12), 125109 (2009). https://doi.org/10.1063/1.3276292

Manes, C., Pokrajac, D., Nikora, V.I., Ridolfi, L., Poggi, D.: Turbulent friction in flows over permeable walls. Geophys. Res. Lett. **38**(3), 03402 (2011). https://doi.org/10.1029/2010GL045695

Manes, C., Poggi, D., Ridolfi, L.: Turbulent boundary layers over permeable walls: scaling and near-wall structure. J. Fluid Mech. **687**, 141–170 (2011). https://doi.org/10.1017/jfm.2011.329

Miller, D.S.: Internal Flow Systems. Bedford, BHRA (Information Services), Cranfield (1990)

Nikuradse, J.: Strömungsgesetze in rauhen Rohren. VDI-Forschungsheft **361** (1933)

Orlandi, P., Leonardi, S., Antonia, R.A.: Turbulent channel flow with either transverse or longitudinal roughness elements on one wall. J. Fluid Mech. **561**, 279–305 (2006). https://doi.org/10.1017/S0022112006000723

Rosti, M.E., Brandt, L., Pinelli, A.: Turbulent channel flow over an anisotropic porous wall - drag increase and reduction. J. Fluid Mech. **842**, 381–394 (2018). https://doi.org/10.1017/jfm.2018.152

Shur, M., Strelets, M., Travin, A., Suzuki, T., Spalart, P.: Unsteady simulations of sound propagation in turbulent flow inside a lined duct. AIAA J. **59**(8), 3054–3070 (2021)

Tanner, P., Gorman, J., Sparrow, R.: Flow-pressure drop characteristics of perforated plates. Int. J. Numer. Methods Heat Fluid Flow **29**(11), 4310–4333 (2019). https://doi.org/10.1108/HFF-01-2019-0065

Vanna, F.D., Picano, F., Benini, E.: A sharp-interface immersed boundary method for moving objects in compressible viscous flows. Comput. Fluids **201**, 104415 (2020). https://doi.org/10.1016/j.compfluid.2019.104415

Wei, H., Gao, D., Zhou, L., Feng, D., Chen, R.: Different combustion modes caused by flame-shock interactions in a confined chamber with a perforated plate. Combust. Flame **178**, 277–285 (2017). https://doi.org/10.1016/j.combustflame.2017.01.011

Weller, H.G., Tabor, G., Jasak, H., Fureby, C.: A tensorial approach to computational continuum mechanics using object-oriented techniques. Comput. Phys. **12**(6), 620–631 (1998). https://doi.org/10.1063/1.168744

Yang, J., Stroh, A., Chung, D., Forooghi, P.: Direct numerical simulation-based characterization of pseudo-random roughness in minimal channels. J. Fluid Mech. **941**, 47 (2022). https://doi.org/10.1017/jfm.2022.331